ACS EARTH AND SPACE CHEMISTRY

http://pubs.acs.org/journal/aesccq

Article

Investigation on Shock Metamorphism of Anatase by Supersonic Microprojectile Impact

Seungyeol Lee, Jizhe Cai, Shiyun Jin, Hiromi Konishi, Dongzhou Zhang, Amanda S. Barnard, Ramathasan Thevamaran, and Huifang Xu*

Cite This: *ACS Earth Space Chem.* 2023, 7, 1905−1915

Read Online

ACCESS | Metrics & More | Article Recommendations | Supporting Information

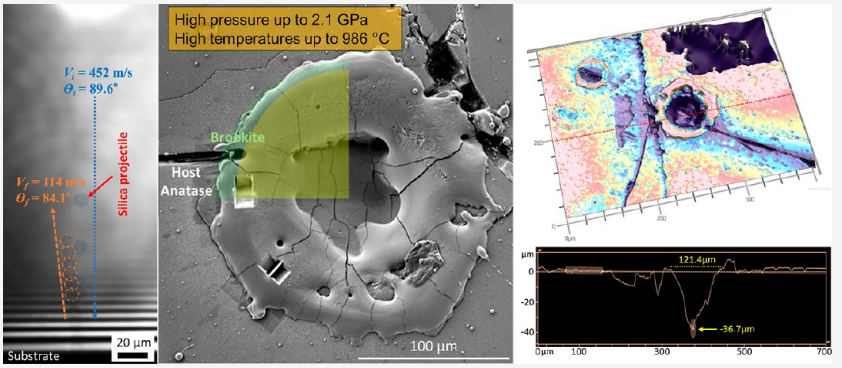

ABSTRACT: The phase relationships of TiO_2 polymorphs are of significance to the field of earth and planetary science, because these phases are crucial geochemical markers of natural shock occurrences and processes that take place in the crust and mantle of planets. In this study, we use a novel method called the laser-induced projectile impact testing (LIPIT) technique to investigate the shock metamorphism of TiO_2 polymorphs by controlled supersonic impacts of microparticles. The 3D digital microscope, synchrotron X-ray diffraction (XRD), focused ion beam/scanning electron microscopy (FIB/SEM), transmission electron microscopy (TEM), and density functional theory calculations are used to investigate and interpret the phase transformations of shocked anatase. The synchrotron XRD and TEM investigations of the impact region show the phase transformation of anatase to rutile, brookite, srilankite, and amorphous TiO_2 phase. According to the impact calculation, the shocked regions experienced a high pressure up to 2.1 GPa and high temperatures up to 986 °C. The shock waves created by impacts are attributed to shock-induced phase changes and lattice dynamic instability. The twinned rutile nanocrystals at the impact area have planar defects following {011} planes that formed under intense pressure or stress. The shearing on the rutile {011} planes can produce the epitaxial nucleation of srilankite at the rutile twin boundary. The methodology of the study, which combines LIPIT microprojectile experiments with simulations and characterization techniques, can help us better understand shock metamorphism in minerals and rocks. It will be helpful for expanding our understanding of the process by which shock metamorphism occurs on planetary bodies, including the Earth, Moon, Mars, and others.

KEYWORDS: *shock metamorphism, LIPIT, anatase, rutile, and srilankite*

1. INTRODUCTION

Titanium dioxide polymorphs are widely distributed as accessory minerals in igneous rocks, metamorphic rocks, mantle xenoliths, lunar rocks, and meteorites.[1−6] Geologists and planetary scientists are interested in the phase relations of these TiO_2 polymorphs due to their potential use as markers for geochemical processes occurring in planetary crusts and mantles as well as natural shock events.[4,7−9] Titanium dioxide polymorphs have also attracted a lot of attention from the scientific community and industrialists as potential materials for a variety of applications, such as catalysts, chemical sensors, dielectric materials, cosmetics, fiber manufacturing, and solar cells.[10−14]

According to theoretical and experimental observations, titanium dioxide can exist in a large variety of structural polymorphs under specific pressure and temperature conditions.[5,15−18] Rutile, anatase, and brookite are the three common polymorphs of TiO_2 that are most prevalent in nature.[15,19,20] Other TiO_2 polymorphs can appear under specific

Received: March 3, 2023
Revised: September 24, 2023
Accepted: September 25, 2023
Published: October 6, 2023

high-pressure and high-temperature conditions, including the orthorhombic scrutinyite-type mineral srilankite (srilankite is a solid solution in the $(Zr,Ti)O_2$ series, also known as α-PbO_2-type TiO_2 and TiO_2-II),[21] the ordered monoclinic mineral riesite,[22] the monoclinic baddeleyite-type mineral akaogiite,[23,24] the cotunnite-type TiO_2 polymorph,[25] the fluorite-type TiO_2 polymorph,[26] and pyrite-type TiO_2 polymorph.[27] The majority of the high-pressure phases transform into srilankite during the decompression process.[9] Srilankite and baddeleyite-type polymorphs are among the high-pressure TiO_2 polymorphs that can be cooled to room temperature.[27−29]

With the discovery of naturally occurring shock-induced TiO_2 polymorphs such as srilankite and riesite, a deep understanding of the TiO_2 phase relations is required to constrain the shocked metamorphic conditions in earth and planetary systems.[22,30,31] In this study, we investigate the shock metamorphism of anatase induced by supersonic microprojectile impacts using a laser-induced projectile impact testing (LIPIT) technique. The LIPIT methodology is a novel approach for testing shock metamorphism on a mineral surface.[32−35] The phase transformation behavior of shocked phases was studied using a 3D digital microscope, synchrotron X-ray diffraction (XRD), focused ion beam/scanning electron microscopy (FIB/SEM), transmission electron microscope (TEM), and density functional theory (DFT) calculations. The structures of the obtained TiO_2 polymorphs are characterized by Rietveld refinement, selected area diffraction patterns (SAED), and high-resolution TEM (HRTEM) with fast Fourier transform (FFT) patterns. The findings of this work offer essential information on the macro-to-nanoscale shock metamorphism of TiO_2 polymorphs under high pressure and temperature environments.

2. METHODS

Shock metamorphism experiments were carried out using the LIPIT technique (Figure 1). Monodisperse spherical silica microprojectiles (~9 μm in diameter) were drop cast on a launchpad, and an ablation laser pulse (8−10 ns pulse duration, 1064 nm wavelength) from a Nd:YAG laser (Quanta-Ray INDI-40-10-HG, Spectra-Physics) was utilized to selectively propel the individual microprojectiles at supersonic speeds. The launchpad is made up of a polydimethylsiloxane (PDMS) layer (Sylgard 184, Dow Chemical) that was spin-coated onto 50 nm thick gold-coated microscope cover glass (210 μm) and cured at 100 °C for an hour. The cured PDMS film had a thickness of around 80 μm. Monodisperse amorphous silica microspheres were drop-cast onto the launchpad, and an inverted microscope was used to align individual or clusters of microspheres to the laser's focal point.

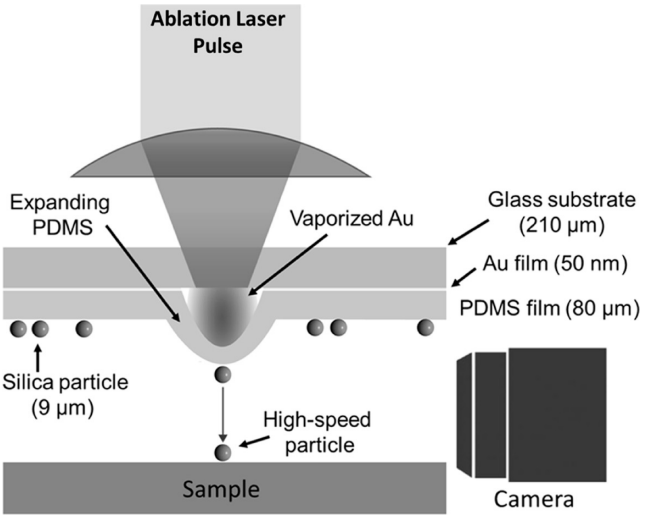

Figure 1. An illustration of the laser-induced single projectile impact experiment. Multiexposure images of a silica projectile in flight were captured at 103 ns intervals using a custom-built ultrahigh speed imaging system. The diameter of the monodisperse spherical silica microprojectiles is approximately 9 μm. The illustration is reproduced from Lee et al. (2020).[33] (Panel A reproduced with permission from ref 33. Copyright 2020, American Chemical Society.)

Silica microspheres were shot selectively at the sample at high speeds using an ablation laser pulse that ablates the thin gold film and quickly expands the PDMS layer. The projectile's launching velocity is dependent on the characteristics of the projectile, ablation laser energy, and the launch pad structure. Recent studies using the same LIPIT technique offer detailed descriptions of the technique.[33−35] The laser energy was tuned for the launch pad we used to be about 0.56 mJ/pulse by utilizing an attenuator to launch the 9 μm silica sphere at 450 m/s. A high-resolution microscope camera (Allied Vision Mako G-234B with OPTEM FUSION 12.5:1 lens) was used to capture images of the projectile in flight at 103 ns intervals by picosecond laser pulses from a supercontinuum white laser (NKT photonics EXR-20) externally shuttered by an acousto-optic modulator.

A 3D laser scanning-confocal microscope (Keyence VK-X1000, Japan) and SEM were used to examine the 3D topographical features of impact regions. SEM observation and preparation of focused-ion-beam (FIB) cross sections for the TEM study were carried out by using FEI Scios dual-beam methods. Secondary electron (SE) images were taken in high vacuum using a sample-to-objective working distance of ~7 mm and a 15 kV accelerating voltage. After identifying regions of interest in the SE images, TEM imaging and selected-area electron diffraction were carried out using an FEI Talos F200X field-emission STEM and Philips CM 200UT microscope operated at 200 kV. The crystal structures and phase identifications of TiO_2 polymorphs were determined by HRTEM images and SAED patterns. As an additional complementary experiment, ball milling of rutile crystals (0.1−0.2 mm size) was carried out using a SPEX high-energy ball mill for 30 min. A drop of the ball-milled powder suspension was placed on a holey-carbon film supported by a TEM Cu grid and air-dried.

Synchrotron radiation XRD patterns of shocked TiO_2 were obtained at beamline 13-BM-C at the Advanced Photon Source (APS), Argonne National Laboratory. The X-ray beam was focused to 12 × 18 μm with Kirkpatrick-Baez mirror and monochromated to 28.6 keV (0.434 Å) with a 1 eV bandwidth. The NIST standard LaB_6 powder was used to calibrate the distance and tilt of the Pilatus3 1 M detector (Dectris), which was positioned 170 mm from the sample. Using an optical microscope, the sample from the impact region was placed on the silica glass capillary. The crystal structures of the obtained TiO_2 polymorphs were determined using the Rietveld method with GSAS II software.[36]

The first-principles computer simulation of the structure and energy of the rutile/srilankite interface was carried out using DFT within the Generalized-Gradient Approximation (GGA), with the exchange−correlation functional of Perdew and Wang.[37] This was performed using the Vienna Ab initio Simulation Package (VASP), which spans reciprocal space with

https://doi.org/10.1021/acsearthspacechem.3c00057
ACS Earth Space Chem. 2023, 7, 1905−1915

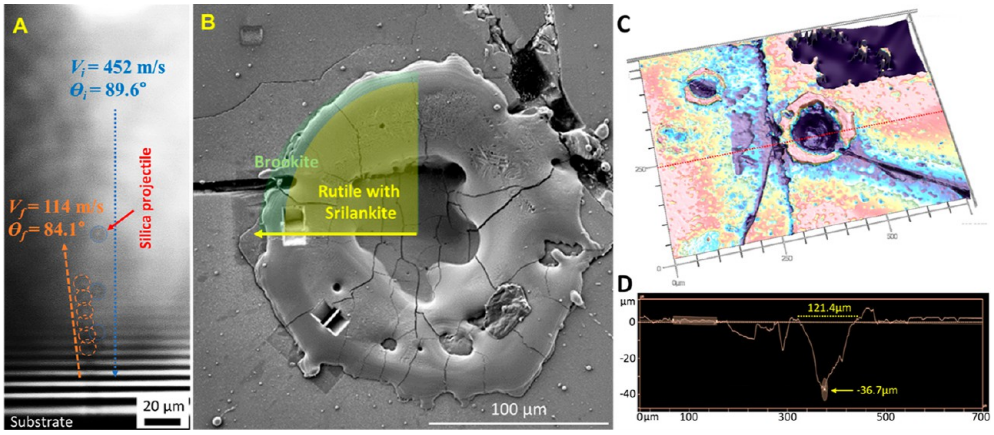

Figure 2. (A) A multiexposure image showing a silica-projectile impacting and bouncing after a laser ablation pulse; (B) a SE image of impacted anatase; (C) 3D topography of impacted areas of anatase from the laser scanning confocal microscope; and (D) optical profilometer trace showing the topography along the red dashed line in part (C).

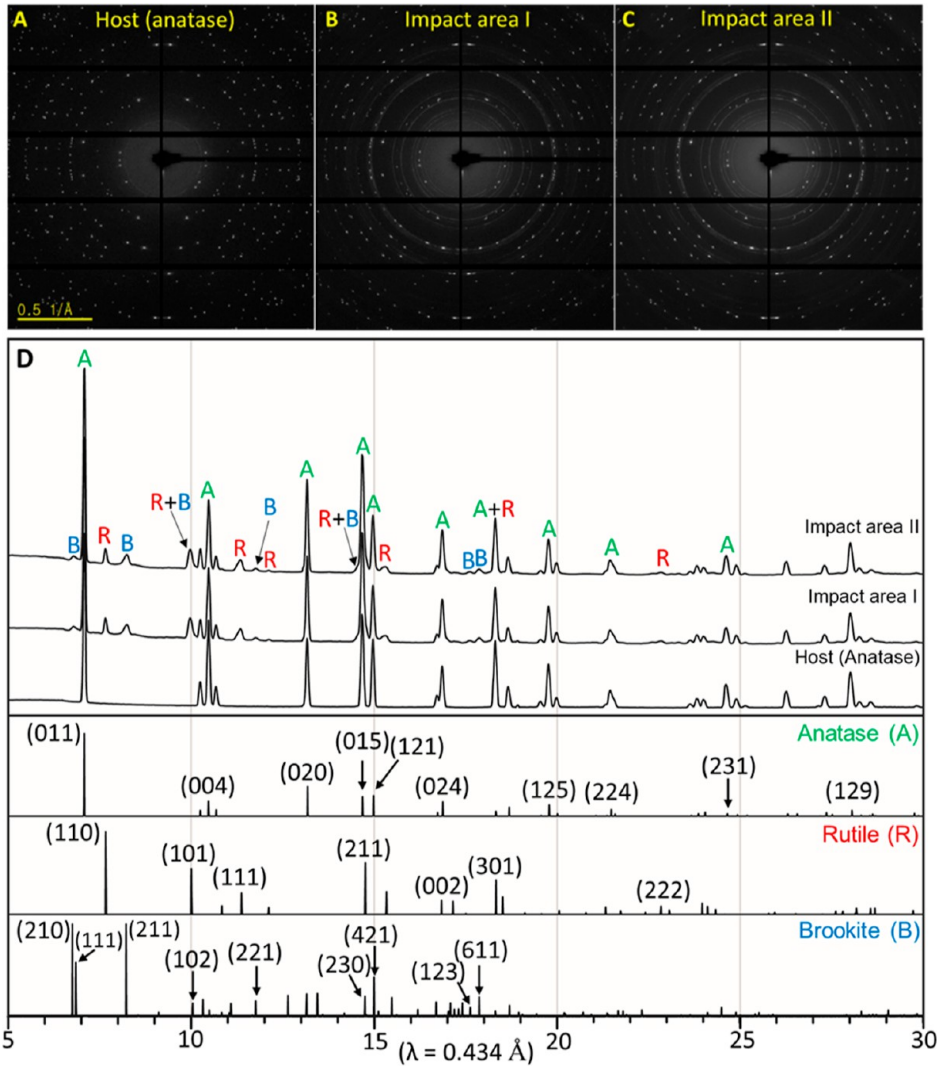

Figure 3. Slice of 2-D image plate from initial anatase diffraction (A) and from impact areas (B,C), and synchrotron radiation XRD pattern of initial anatase and two impacted areas (D), compared to anatase, rutile, and brookite as reference minerals.[47,48] Diffraction rings from both rutile and brookite are continuous because of their extremely small crystal sizes and random orientations.

a plane-wave basis set and a relaxation technique involving an efficient matrix-diagonalization routine based on a sequential band-by-band residual minimization method of single-electron energies with direct inversion in the iterative subspace.[38,39] To improve the computational accuracy, the structural relaxations and interface structure, as well as the final calculations of the

https://doi.org/10.1021/acsearthspacechem.3c00057
ACS Earth Space Chem. 2023, 7, 1905−1915

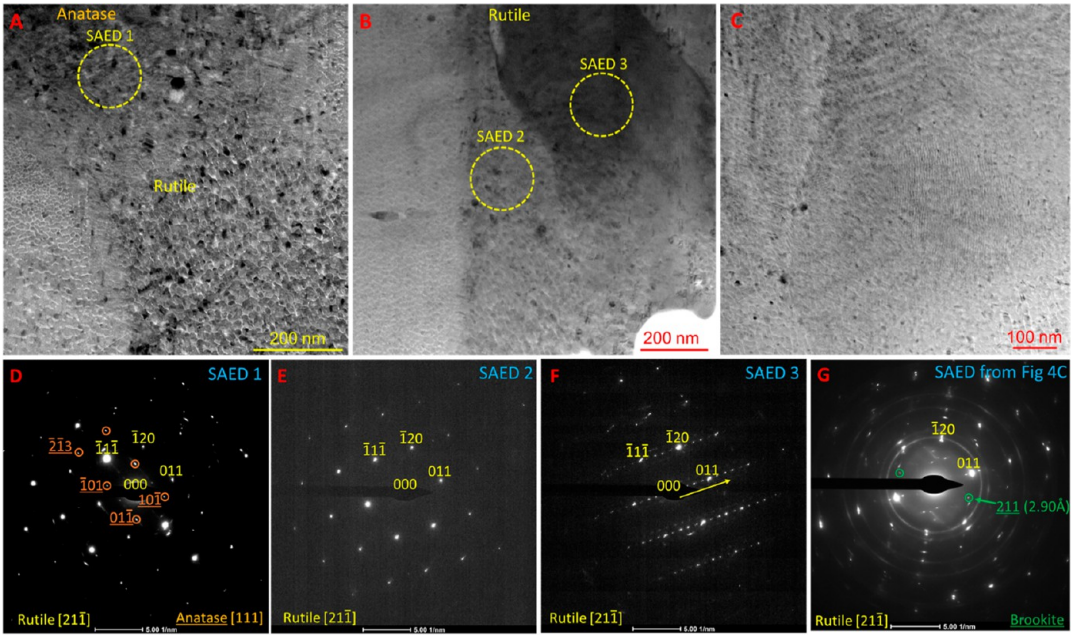

Figure 4. Bright-field TEM images of the shocked anatase area (A−C), with their SAED patterns (D−G). The initial anatase, rutile, and brookite are identified in the SAED.

interface energy, were performed using the Projected Augmented Wave (PAW) potentials[40] and reciprocal-space projected wave functions to a convergence of 10^{-4} eV. PAW potentials are generally considered to be more accurate than the ultrasoft pseudopotentials,[41] since PAW potentials reconstruct the exact valence wave function with all nodes in the core region. This technique has already been successfully used to calculate the elastic properties of the anatase and rutile phases of TiO_2 and to study the structure, energy, and surface stress of the low-index surfaces of anatase and rutile with various types of surfactants.[42,43]

3. RESULTS

The silica projectile's impact speed and angle were captured on a high-resolution microscope camera with an ultrafast multi-exposure imaging technique (Figure 1). The silica projectile was accelerated to a velocity of approximately 452 m/s (Figure 2A). The rebound speed of the projectile is about 114 m/s (Figure 2A). The topographical features reveal important details about impact mechanisms, including physical and geological processes.[44,45] The morphology of the impact crater was investigated by using a three-dimensional laser scanning confocal microscope and SE image (Figure 2B−D). Craters and surface melts were created by projectile impact and laser ablation (Figure 2B). The morphology of the crater, which has a raised rim and a depth-to-diameter ratio of around 1/3 (Figure 2D), is similar to that of meteorite impact craters.[46]

High-quality spatially resolved micro-XRD patterns of host anatase and impacted regions were obtained using synchrotron X-ray scattering (Figure 3). The diffraction peaks of the initial anatase show a pure TiO_2 phase (Figure 3A,D). Diffraction patterns of the impact areas show the phase transformation from anatase to rutile and brookite (Figure 3). The major peaks at 3.249, 2.496, and 2.193 Å are associated with those from rutile, and the peaks at 3.650 and 3.020 Å are associated with those from brookite (Figure 3D). The Scherrer Equation[49] is used to determine the crystallite sizes of rutile and brookite from impact area II (Figure 3). The estimated crystallite sizes of the impacted rutile, which come from (110), (101) and (111) peaks, are 51.5(3.8), 38.8(1.2), and 33.1(2.0) nm, respectively. Rutile's (110) peak is noticeably sharper than other (*hkl*) peaks, suggesting platelike shapes or domains caused by stacking faults under high pressure or stress. The brookite's estimated crystallite sizes from its (211), (210) and (111) peaks are 29.5 (1.8), 24.1 (2.7), and 22.5 (2.9) nm, respectively.

A combination of the bright-field TEM images, TEM-EDS maps, SAED patterns, HRTEM images, and fast Fourier transform (FFT) patterns were used to characterize the TiO_2 polymorphs in the impact area of the FIB section (Figures 4, 5, and S1). According to the TEM-EDS examination, the impact area is primarily composed of TiO_2 with the presence of minor amounts of Fe in some areas (Figure S1). The bright-field TEM images show a variety of nanocrystalline and irregular grain boundaries in the TiO_2 polymorphs (Figure 4A−C). SAED patterns identified the [21$\bar{1}$]-zone-axis of rutile and the [111]-zone-axis of anatase in the FIB section (Figure 4D−G). A (211) reflection of the brookite phase is identified in the SAED pattern of the rutile dominant area (Figure 4G).

Nanoscale amorphous TiO_2 phases formed at certain shocked rutile areas (Figure 5A). HRTEM images and FFT patterns from the shocked rutile domains exhibit periodic twinning along ⟨011⟩ directions (Figure 5B). A high-pressure phase of TiO_2 with the srilankite-type structure has been identified in the twinned rutile domains (Figure 5B). The (002) plane of srilankite is parallel to the (011) twin plane of rutile, as shown in the specific crystallographic relationship between $[210]_{srilankite}$ and $[21\bar{1}]_{rutile}$ (Figures 5B−E). A srilankite phase has been found in a severely damaged impact area that displays the [111]-zone-axis in the FFT pattern (Figure 5F).

In order to better understand the relationship between twinned rutile and srilankite, we have also studied the pressure-induced structural change of rutile by a ball-milled experiment. Similar to the microprojectile impacts experiment, the results of the TEM images reveal that strong forces from ball-milling can cause rutile crystals to become twinned along ⟨011⟩ directions

https://doi.org/10.1021/acsearthspacechem.3c00057
ACS Earth Space Chem. 2023, 7, 1905−1915

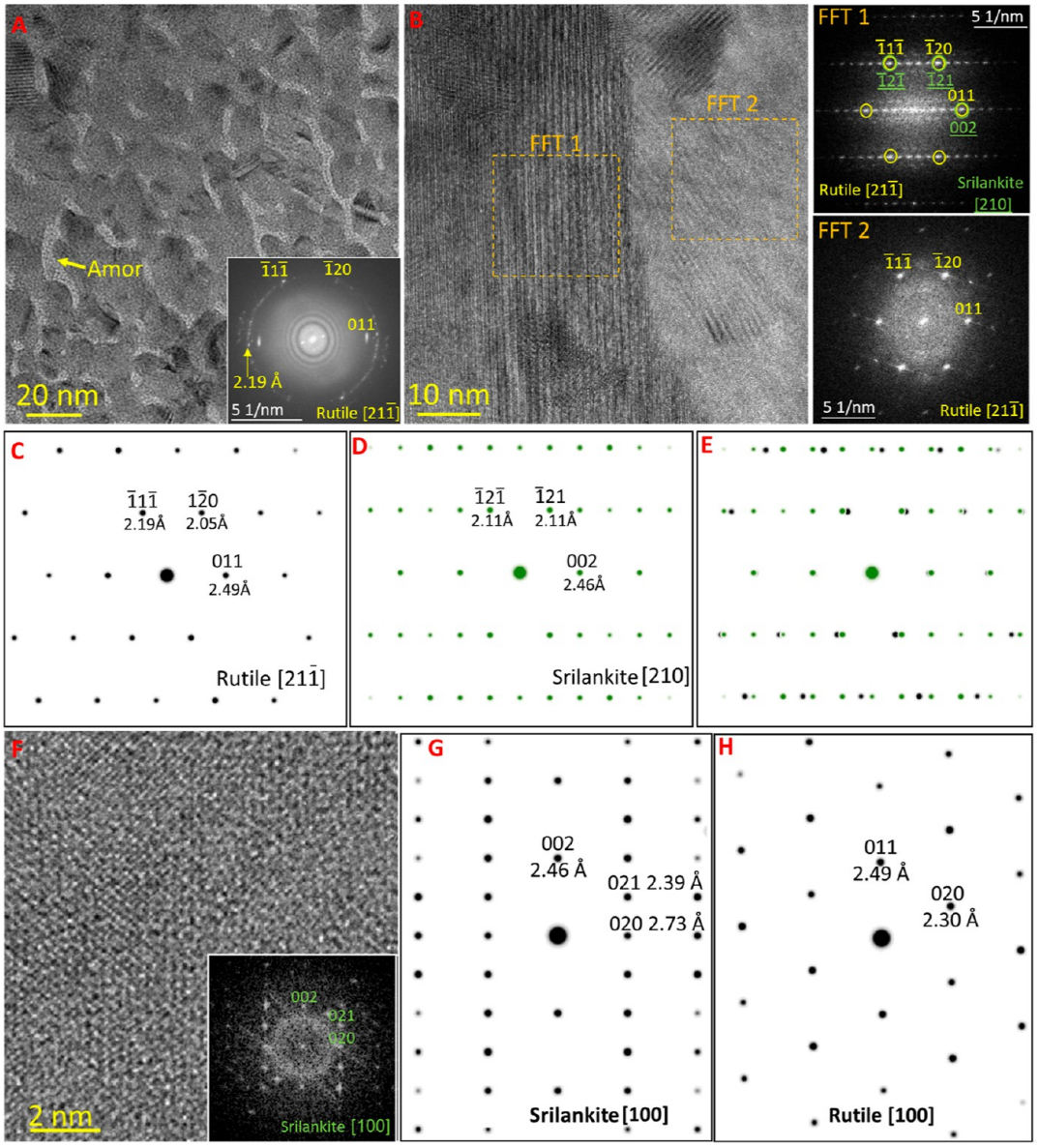

Figure 5. (A) HRTEM images of the shocked rutile area showing the nanoscale amorphous TiO_2 phases; (B) HRTEM images showing twinned rutile area with FFT patterns; (C−E) simulated diffraction patterns in the specific crystallographic relationship at the [210]-zone-axis of srilankite, the [21$\bar{1}$]-zone-axis of rutile, and their overlapped patterns; and (F−H) HRTEM images from the highly damaged area showing the [100]-zone-axis of srilankite.

(Figure 6). The structure at the twin boundary indicates the presence of a unit-cell scale lamella of srilankite (Figure 6B,C). Simulated diffraction patterns of rutile and twinned rutile are shown in Figure 6D,E.

4. IMPACT PRESSURE AND TEMPERATURE

When a microprojectile impacts a material, the area in front of the projectile always experiences maximum pressure and temperature. Using the Rankine−Hugoniot relation, which is derived from the law of conservation of momentum, $P = \rho_0 U_s U_p$, where P, ρ_0, U_s, U_p are the pressure, initial density, shock wave velocity, and particle velocity, we can approximately calculate the pressure during the initial impact close to this region. The equation of state that links the particle velocity to the shock velocity is $U_s = C_0 + SU_p$, where S is the quantity that has been observed experimentally. The particle velocities on either side of the impact interface are calculated, taking into account the pressure equilibrium, $P_1 = P_2$ between the projectile (P_1) and target materials (P_2), and material properties for the projectile and target material. When continuity is assumed, the particle velocity in the target material will be calculated using the formula $V = U_{p1} + U_{p2}$, where V is the projectile's impact speed. The estimated pressure that was produced when the projectile hit anatase at 450 m/s is 2.1 GPa (see supplementary text in the Supporting Information).[5,30,50] Within the impact area, it is expected that there will be a temperature increase of roughly 986 °C. The total temperature increase of the material within the strike area is caused by both laser heating and impact-induced heating, which results in increases of 517 °C (0.056 mJ from 10% laser leakage) and 449 °C, respectively.[51−53]

5. DISCUSSIONS

Rutile, anatase, and brookite are the three commonly occurring polymorphs of titanium dioxide that exist at atmospheric pressure.[3,19] Rutile is a stable phase, while anatase and brookite are both metastable. The high-pressure phases of TiO_2 include

https://doi.org/10.1021/acsearthspacechem.3c00057
ACS Earth Space Chem. 2023, 7, 1905−1915

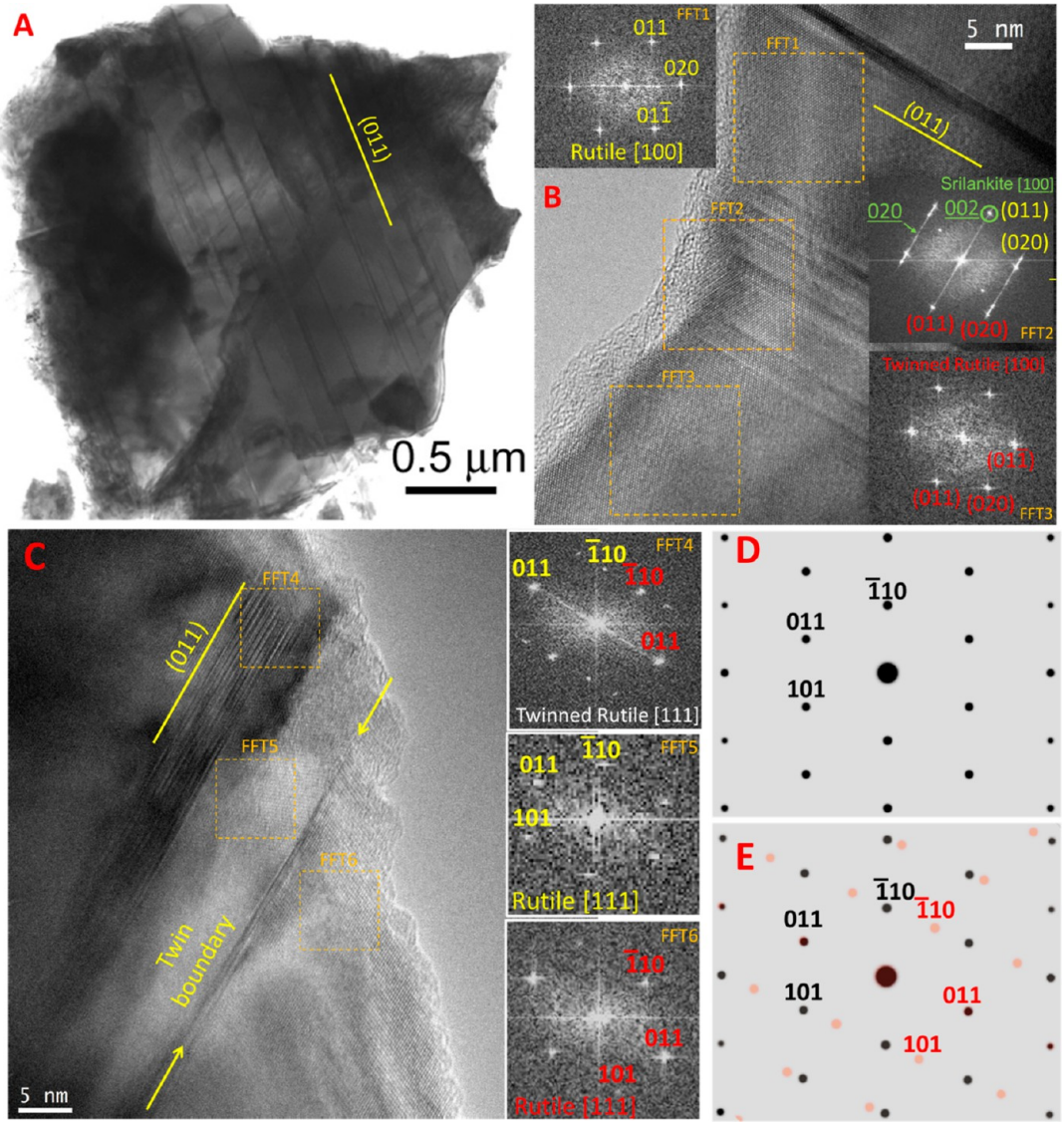

Figure 6. (A) Bright-field TEM image showing dense planar defects, (B,C) HRTEM images of a ball-milled rutile crystal with their FFT patterns, and (D,E) simulated diffraction pattern of rutile's (011) twinning that corresponds to the FFT patterns from (C).

the orthorhombic polymorphs of srilankite, riesite, akaogiite, cotunnite-type, fluorite-type, and pyrite-type polymorphs.[9,21,31] On the stability of these TiO_2 phases, numerous publications have been reported.[5,18,31,55−57]

The anatase, rutile, and brookite at the impact area were detected by the synchrotron XRD technique (Figure 3). The crystal structures of shocked anatase, rutile, and brookite from impact area II were determined by the Rietveld method (Figure 7). As the starting structures for the Rietveld refinement, anatase,[48] rutile, and brookite[47] were used. Fractional coordinates, occupancies, and isotropic displacement parameters of each atom from the refined structure are listed in Table 1. The refined unit-cell parameters, bond distances, and density of anatase, rutile, and brookite are compared to those reported in previous investigations in Table S1. Our refined unit-cell parameters and bond distances are in agreement with those determined by previous studies.[47,48,54,55] The refined brookite structure shows more regular TiO_6 octahedra than that in an early reported structure.[43] The T position of Ti is at the centers of regular octahedra (Table S1). In shocked TiO_2 polymorphs,

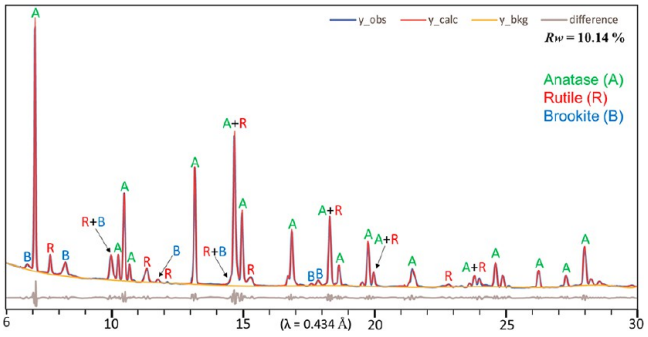

Figure 7. Experimental and calculated synchrotron XRD patterns (overlapped black and red lines) of the studied sample consisting of anatase, rutile, and brookite. The residue (gray line) between the experimental data and calculated profile is shown below the XRD pattern.

the U_{iso} values for Ti atoms are smaller than the U_{iso} values for O atoms (Table 1).

https://doi.org/10.1021/acsearthspacechem.3c00057
ACS Earth Space Chem. 2023, 7, 1905−1915

Table 1. Unit-Cell Parameters, Atomic Coordinates, and Thermal Displacement Parameters (U_{iso}) of Anatase, Rutile, and Brookite from Figure 7

anatase (space group $I4_1/amd$)				
atom	x	y	z	U_{iso} (Å^2)
Ti	0	0	0	0.003(1)
O	0	0	0.2077(3)	0.007(2)
lattice parameters: a = 3.7862(4) and c = 9.5116(9) Å				
rutile (space group $P4_2/mnm$)				
atom	x	y	z	U_{iso} (Å^2)
Ti	0	0	0	0.004(2)
O	0.3043(3)	0.3043(3)	0	0.005(2)
lattice parameters: a = 4.5953(5) and c = 2.9730(3) Å				
brookite (space group $Pbca$)				
atom	x	y	z	U_{iso} (Å^2)
Ti	0.1291(2)	0.1087(2)	0.8759(6)	0.005(1)
O	0.0139(1)	0.1437(2)	0.1850(2)	0.006(2)
O	0.2305(3)	0.1119(2)	0.5411(4)	0.007(2)
lattice parameters: a = 9.1905(7), b = 5.4733(5) and c = 5.1685(4) Å				

The TEM analyses indicate the phase transformation of anatase to rutile, brookite, srilankite, and amorphous TiO_2 phase induced by the microprojectile impact (Figures 4 and 5). A similar result was observed from high-energy ball milling experiments.[56−58] In the early stages of the ball milling process, rutile is the predominant product from anatase, while other phases, such as srilankite and the amorphous phase, are much less common in the TEM samples. High-intensity ball milling of anatase, with an estimated 1 GPa or higher, results in ultrafine rutile crystallites with significant quantities of defects, amorphization of TiO_2, and formation of srilankite (Figure 6). Other milling experiments showed the phase transformation from anatase to rutile via brookite.[59,60] The {112} anatase twin interfaces contain one unit cell of brookite, suggesting that brookite can form at twin planes.[61]

The structures of rutile, anatase, brookite, and srilankite are illustrated in Figure 8. The temperature−pressure phase diagram showing relationships among anatase, rutile, and srilankite is shown in Figure 9. Under the conditions of the given temperature and pressure, brookite is always the least stable phase.[62] The phase diagram shows that anatase can change into rutile at high temperatures and srilankite at high pressures. Normal shock estimates for the supersonic spherical silica projectiles suggest that the shocked regions may have been

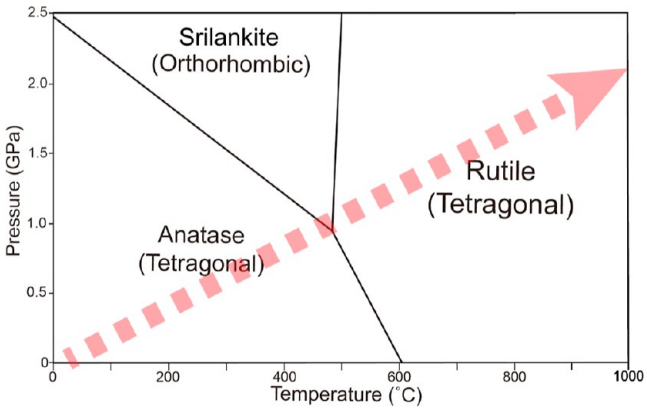

Figure 9. Temperature−pressure phase diagram of anatase, rutile, and srilankite was redrawn based on results from Murray and Wriedt (1987).[16] The red dotted line, which represents an estimated shocked pathway, was subjected to high pressures of up to 2.1 GPa and temperatures as high as 986 °C.

exposed to pressures of up to 2.1 GPa and a temperature rise of up to 986 °C. The triple point for anatase, rutile, and srilankite is estimated to be 1.0 GPa at 480 °C (Figure 9). According to previous studies,[57,63] when defect density and lattice distortion increase, anatase could transform into srilankite at pressures lower than 1 GPa. In these experiments, there are two most likely scenarios for srilankite formation: first, rutile forms during shock compression to 2.1 GPa and then transforms back into srilankite upon release; second, srilankite forms directly from anatase in off-center regions of impact damage where pressure did not reach the stability field of rutile (Figure 9).

The phase transition of anatase to rutile has attracted the interest of several research teams because it serves as a useful indicator for geochemical processes in the Earth's crust and mantle and a variety of industrial applications such as pigments and photocatalysts.[64−67] The reported transformation temperatures range from 375 to 660 °C according to a variety of technologies and processing procedures.[48,66,68] As a result, rutile is commonly found in the rocks, ashes, and soils that are the result of volcanic activity.[1,6,19] The anatase to rutile transformation is reconstructive, meaning that linkages are broken and then rebuilt during the process.[28,65]

In our experiment, anatase changed into rutile due to shock impact and heat produced by projectile impact and laser ablation (Figures 3−5). The primary cause of shock-induced phase

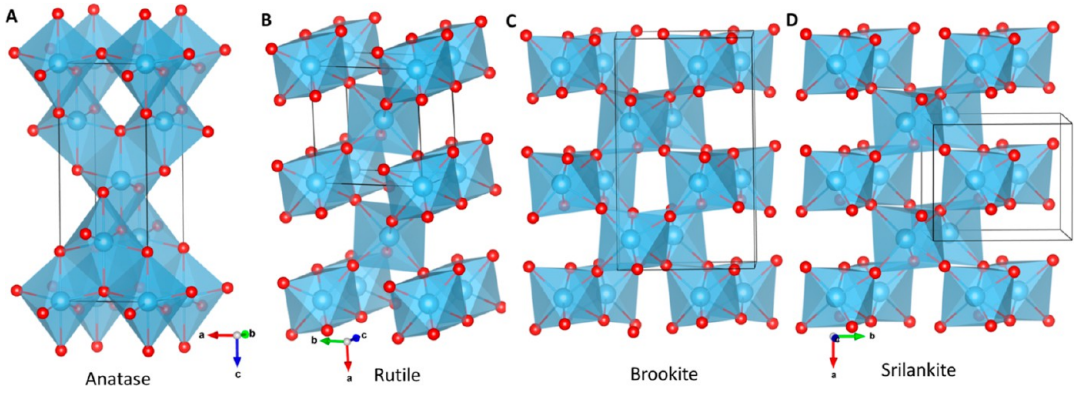

Figure 8. Structural models of anatase (A), rutile (B), brookite (C), and srilankite (D). The structure of anatase, rutile, and brookite calculated from Rietveld refinement. Sky blue atoms are titanium, and red atoms are oxygen.

https://doi.org/10.1021/acsearthspacechem.3c00057
ACS Earth Space Chem. 2023, 7, 1905−1915

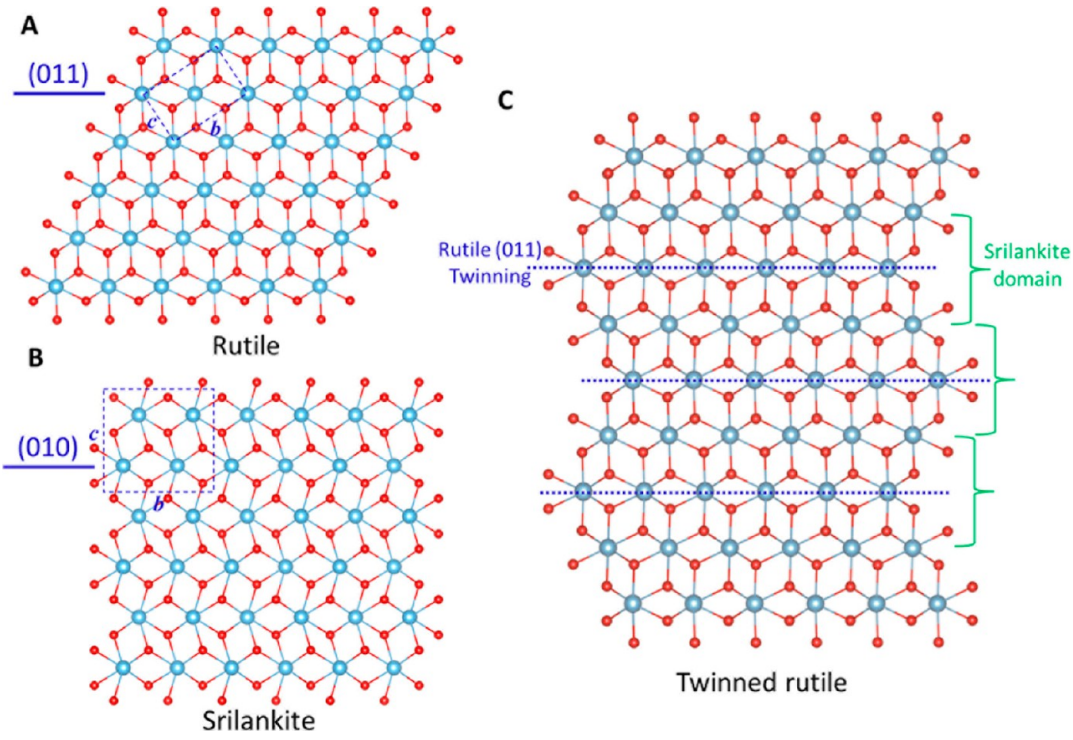

Figure 10. Schematic diagram of rutile (A), srilankite (B), and the srilankite layers at the rutile twin boundary (C). Sky blue atoms are titanium, and red atoms are oxygen.

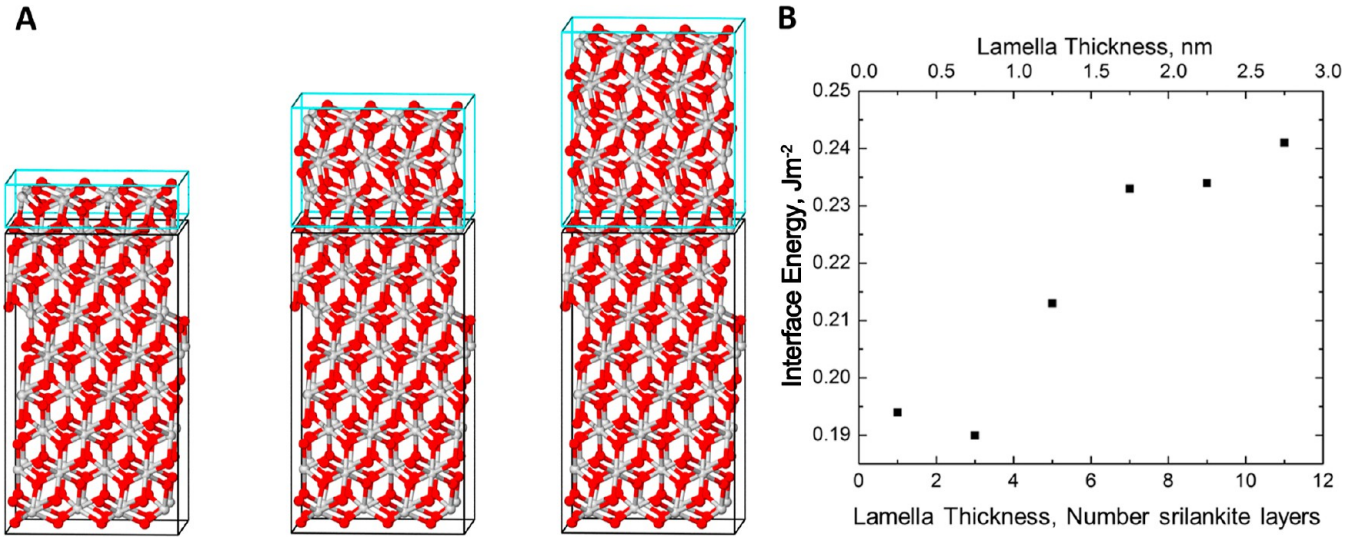

Figure 11. (A) Periodic supercells used to calculate the formation energy for srilankite lamella in rutile TiO_2. The rutile layer is highlighted by the black box; and the srilankite layer by the blue box. Note that the smallest structure (left) is effectively a rutile (011) extrinsic planar defect observed in the HRTEM images. (B) Calculated results showing the interface energy between host phase rutile and srilankite lamella.

transformation of anatase to rutile is considered to be the volume shrinkage of anatase caused by lattice dynamical instabilities brought on by impact-induced shock waves.[4,30,31] Rutile has a larger octahedral tilt than anatase, which results in a denser and more compressible structure (Table S1). A complex, highly deformed nanostructure and polycrystalline aggregates of the shocked rutile were observed in the TEM images (Figure 4). The broad diffraction peaks of shocked rutile (Figure 3D) also indicate a large number of defects that are responsible for the nanoscale domains seen in the TEM images (Figures 4 and 5). The shocked rutile grains appear as twinned nanocrystals with planar defects in the ⟨011⟩ directions when seen along the [211]-zone-axis (Figure 5). The twinning of rutile on the (011) plane, which occurs frequently in crustal rocks, is known as geniculated twinning.[69]

The structure at rutile's (011) twin boundary corresponds to a unit-cell scale lamella with a srilankite structure (Figure 10). Figure 10C illustrates how this enables the epitaxial nucleation of srilankite at the rutile's twin planes.[7,9] In nature, shocked rutile and srilankite have been identified in ultrahigh-pressure diamond-bearing gneiss,[7] shocked gneiss from suevitic breccia of the Ries impact crater,[70] coesite-bearing eclogite,[71] and breccias from the late Eocene Chesapeake Bay impact structure.[4] The srilankite phase may serve as a useful *P*-T

https://doi.org/10.1021/acsearthspacechem.3c00057
ACS Earth Space Chem. 2023, 7, 1905−1915

indicator of subduction of continental crust to the transition zone of the mantle.[72]

We also carried out preliminary calculations from first-principles using DFT within the generalized-Gradient approximation (GGA) to examine the thermodynamic stability of the α-PbO_2-type lamella in rutile. Using this approach, the formation energies for bulk rutile and bulk srilankite (a = 4.492 Å, b = 5.468 Å, and c = 4.911 Å) were also calculated, by subtracting the enthalpies for the bulk titanium metal and oxygen (from O_2) from the respective compounds. The free energy difference could also be determined using the entropy as demonstrated elsewhere[73] or calculated using the QuickThermo software package,[74] but at the same temperature and pressure the energy difference will be similar.

To predict the interfacial energy between rutile and srilankite, the formation energy was calculated for a series of periodic bulk structures by successively increasing the thickness of an α-PbO_2-type or a srilankite layer (Figure 11A). In each case, the thickness of the underlying (011) rutile layer has been set to a constant value of 1.83 nm, and the equilibrium lattice parameters of rutile have been used. Hence, the α-PbO_2-type layer is strained to accommodate the rutile structure. The results show that the 2-dimensional interface energy is directly related to the lamella thickness (Figure 11B), and distortions of the srilankite lattice can lower the energy when the lamella are thin. As the lamella increases in thickness, the interfacial energy converges to a higher value as the srilankite structure is imposed and the lattice distortions can no longer be accommodated. The difference of ΔE = 25.91 kJ mol^{-1} in favor of rutile confirms rutile as the low energy polymorph, and establishes the formation energy of srilankite interfaces relative to this baseline.

6. CONCLUSIONS

Supersonic microprojectile impact experiments using the LIPIT technique are a novel tool to study the shock metamorphism of minerals and rocks. The main advantage of the LIPIT technique is its ability to provide dynamic tests at smaller length scales and to control the projectile size and impact speed.[34,50,75] Thus, the LIPIT technique could be used to recreate collision situations in the lab for rock-forming minerals under various experimental settings by varying the projectiles' density, speed, and angles and study the impact induced deformation processes holistically from macroscale cratering to atomistic scale phase transformations and crystal defects. The LIPIT technique was successfully used by Lee et al. (2020)[33] to investigate the phase transformation of opal-A to coesite. In this study, the shock metamorphism of anatase induced by supersonic microprojectile impacts was investigated using a three-dimensional laser scanning confocal microscope, synchrotron XRD and TEM. The result showed that at pressures up to 2.1 GPa and temperatures up to 986 °C, anatase experienced a phase transformation into rutile, brookite, the amorphous TiO_2 phase, and srilankite. The lattice dynamic instabilities driven by the impact-induced shock waves could be the main reason for the phase transformation. Epitaxial nucleation of srilankite results from planar defects on the rutile's (011) plane at the twin boundary. In summary, the integrated LIPIT microprojectile tests, electron microscopy imaging, synchrotron characterization, and first-principles DFT calculations will be useful in understanding shock metamorphism in minerals and rocks. The integrated approach will improve our understanding of shock metamorphism on Earth, Moon, Mars, and other planetary bodies.

■ ASSOCIATED CONTENT

Supporting Information

The Supporting Information is available free of charge at https://pubs.acs.org/doi/10.1021/acsearthspacechem.3c00057.

Estimation of impact-induced pressure and temperature rise; TEM images of focused ion beam (FIB) section from shocked anatase area; and comparison of unit-cell parameters, bond distances, and density of brookite, rutile, and anatase (PDF)

■ AUTHOR INFORMATION

Corresponding Author

Huifang Xu − *Department of Geoscience, University of Wisconsin—Madison, Madison, Wisconsin 53706, United States;* orcid.org/0000-0002-7464-0057; Email: hfxu@geology.wisc.edu

Authors

Seungyeol Lee − *Department of Geoscience, University of Wisconsin—Madison, Madison, Wisconsin 53706, United States; Department of Earth and Environmental Sciences, Chungbuk National University, Cheongju 28644, Republic of Korea*

Jizhe Cai − *Department of Mechanical Engineering, University of Wisconsin—Madison, Madison, Wisconsin 53706, United States;* orcid.org/0000-0003-2803-2111

Shiyun Jin − *Department of Geoscience, University of Wisconsin—Madison, Madison, Wisconsin 53706, United States; Gemological Institute of America, Carlsbad, California 92008, United States*

Hiromi Konishi − *Department of Geoscience, University of Wisconsin—Madison, Madison, Wisconsin 53706, United States;* Present Address: Department of Geology, Niigata University, 8050 Ikarashi 2-no-cho, Nishi-ku 12 Niigata 950-2181, Japan

Dongzhou Zhang − *GeoSoilEnviroCARS, University of Chicago, Lemont, Illinois 60439, United States; Hawaii Institute of Geophysics & Planetology, School of Ocean and Earth Science and Technology, University of Hawaii, Honolulu, Hawaii 96822, United States;* orcid.org/0000-0002-6679-892X

Amanda S. Barnard − *School of Computing, Australia National University, Canberra, ACT 2601, Australia;* orcid.org/0000-0002-4784-2382

Ramathasan Thevamaran − *Department of Mechanical Engineering, University of Wisconsin—Madison, Madison, Wisconsin 53706, United States;* orcid.org/0000-0001-5058-6167

Complete contact information is available at: https://pubs.acs.org/10.1021/acsearthspacechem.3c00057

Notes

The authors declare no competing financial interest.

■ ACKNOWLEDGMENTS

Authors thank Dr. Yang Li and Dr. Yiping Yang for help on preparing FIB TEM samples and part of TEM observation. J.C. and R.T. acknowledge the support from the U.S. Office of Naval Research under PANTHER award number N000142112916 through Dr. Timothy Bentley. The authors acknowledge NASA Astrobiology Institute (NNA13AA94A) for supporting this

study. Part of this work was performed at GeoSoilEnviroCARS (Sector 13), Partnership for Extreme Crystallography program (PX̂2), Advanced Photon Source (APS), and Argonne National Laboratory. This work was supported by the research grant of the Chungbuk National University in 2023. GeoSoilEnviroCARS is supported by the National Science Foundation-Earth Sciences (EAR-1634415) and Department of Energ-Geosciences (DE-FG02-94ER14466). PX̂2 program is supported by COMPRES under NSF Cooperative Agreement EAR-1661511. Authors acknowledge valuable comments and suggestions from Prof. Sumit Chakraborty and an anonymous reviewer.

REFERENCES

(1) Buseck, P. R.; Keil, K. Meteoritic Rutile. *Am. Mineral.* **1966**, *51* (9−10), 1506−1515.
(2) Hlava, P. F.; Prinz, M.; Keil, K. Niobian Rutile in an Apollo 14 Kreep Fragment. *Meteoritics* **1972**, *7* (4), 479−486.
(3) Banfield, J. F.; Bischoff, B. L.; Anderson, M. A. TiO_2 Accessory Minerals: Coarsening, and Transformation Kinetics in Pure and Doped Synthetic Nanocrystalline Materials. *Chem. Geol.* **1993**, *110* (1−3), 211−231.
(4) Jackson, J. C.; Horton, J. W.; Chou, I.-M.; Belkin, H. E. A Shock-Induced Polymorph of Anatase and Rutile from the Chesapeake Bay Impact Structure, Virginia, U.S.A. *Am. Mineral.* **2006**, *91* (4), 604−608.
(5) Smith, S. J.; Stevens, R.; Liu, S.; Li, G.; Navrotsky, A.; Boerio-Goates, J.; Woodfield, B. F. Heat Capacities and Thermodynamic Functions of TiO_2 Anatase and Rutile: Analysis of Phase Stability. *Am. Mineral.* **2009**, *94* (2−3), 236−243.
(6) Meinhold, G. Rutile and Its Applications in Earth Sciences. *Earth-Sci. Rev.* **2010**, *102* (1−2), 1−28.
(7) Hwang, S. L.; Shen, P.; Chu, H. T.; Yui, T. F. Nanometer-Size Alpha-PbO_2-Type TiO_2 in Garnet: A Thermobarometer for Ultrahigh-Pressure Metamorphism. *Science* **2000**, *288* (5464), 321−324.
(8) Bromiley, G. D.; Redfern, S. A. T. The Role of TiO_2 Phases during Melting of Subduction-Modified Crust: Implications for Deep Mantle Melting. *Earth Planet. Sci. Lett.* **2008**, *267* (1−2), 301−308.
(9) Chen, M.; Gu, X.; Xie, X.; Yin, F. High-Pressure Polymorph of TiO_2-II from the Xiuyan Crater of China. *Chin. Sci. Bull.* **2013**, *58* (36), 4655−4662.
(10) Cao, L.; Gao, Z.; Suib, S. L.; Obee, T. N.; Hay, S. O.; Freihaut, J. D. Photocatalytic Oxidation of Toluene on Nanoscale TiO_2 Catalysts: Studies of Deactivation and Regeneration. *J. Catal.* **2000**, *196* (2), 253−261.
(11) Hara, K.; Sayama, K.; Arakawa, H.; Ohga, Y.; Shinpo, A.; Suga, S. A Coumarin-Derivative Dye Sensitized Nanocrystalline TiO_2 Solar Cell Having a High Solar-Energy Conversion Efficiency up to 5.6%. *Chem. Commun.* **2001**, No. 6, 569−570.
(12) Auffan, M.; Pedeutour, M.; Rose, J.; Masion, A.; Ziarelli, F.; Borschneck, D.; Chaneac, C.; Botta, C.; Chaurand, P.; Labille, J.; Bottero, J.-Y. Structural Degradation at the Surface of a TiO_2-Based Nanomaterial Used in Cosmetics. *Environ. Sci. Technol.* **2010**, *44* (7), 2689−2694.
(13) Roy, P.; Berger, S.; Schmuki, P. TiO_2 Nanotubes: Synthesis and Applications. *Angew. Chem., Int. Ed.* **2011**, *50* (13), 2904−2939.
(14) Nakata, K.; Fujishima, A. TiO_2 Photocatalysis: Design and Applications. *J. Photochem. Photobiol., C* **2012**, *13* (3), 169−189.
(15) Jamieson, J. C.; Olinger, B. Pressure-Temperature Studies of Anatase, Brookite Rutile, and TiO_2(II): A Discussion. *Am. Mineral.* **1969**, *54* (9−10), 1477−1481.
(16) Murray, J. L.; Wriedt, H. A. The O-Ti (Oxygen-Titanium) System. *J. Phase Equilib.* **1987**, *8* (2), 148−165.
(17) Muscat, J.; Swamy, V.; Harrison, N. M. First-Principles Calculations of the Phase Stability of TiO_2. *Phys. Rev. B: Condens. Matter Mater. Phys.* **2002**, *65* (22), 224112.
(18) Kojitani, H.; Yamazaki, M.; Kojima, M.; Inaguma, Y.; Mori, D.; Akaogi, M. Thermodynamic Investigation of the Phase Equilibrium Boundary between TiO_2 Rutile and Its α-PbO_2-Type High-Pressure Polymorph. *Phys. Chem. Miner.* **2018**, *45* (10), 963−980.
(19) Dachille, F.; Simons, P. Y.; Roy, R. Pressure-Temperature Studies of Anatase, Brookite, Rutile and TiO_2-II. *Am. Mineral.* **1968**, *53* (11−12), 1929−1939.
(20) Morad, S. SEM Study of Authigenic Rutile, Anatase and Brookite in Proterozoic Sandstones from Sweden. *Sediment. Geol.* **1986**, *46* (1−2), 77−89.
(21) Willgallis, A.; Siegmann, E.; Hettiaratchi, T. Srilankite, a new Zr-Ti-oxide mineral. *Neues Jahrb. Mineral., Monatsh.* **1983**, *4*, 151−157.
(22) Tschauner, O.; Ma, C.; Lanzirotti, A.; Newville, M. G. Riesite, a New High Pressure Polymorph of TiO_2 from the Ries Impact Structure. *Minerals* **2020**, *10* (1), 78.
(23) El Goresy, A.; Dubrovinsky, L.; Gillet, P.; Graup, G.; Chen, M. Akaogiite: An Ultra-Dense Polymorph of TiO_2 with the Baddeleyite-Type Structure, in Shocked Garnet Gneiss from the Ries Crater, Germany. *Am. Mineral.* **2010**, *95* (5−6), 892−895.
(24) Sato, H.; Endo, S.; Sugiyama, M.; Kikegawa, T.; Shimomura, O.; Kusaba, K. Baddeleyite-Type High-Pressure Phase of TiO_2. *Science* **1991**, *251* (4995), 786−788.
(25) Dubrovinskaia, N. A.; Dubrovinsky, L. S.; Swamy, V.; Ahuja, R. Cotunnite-structured titanium dioxide. *High Pressure Res.* **2002**, *22* (2), 391−394.
(26) Tsai, M. H.; Shen, P.; Chen, S. Y. Defect generation of anatase nanocondensates via coalescence and transformation from dense fluorite-type TiO_2. *J. Appl. Phys.* **2006**, *100* (11), 114313.
(27) Mattesini, M.; De Almeida, J. S.; Dubrovinsky, L.; Dubrovinskaia, N.; Johansson, B.; Ahuja, R. High-pressure and high-temperature synthesis of the cubic TiO_2 polymorph. *Phys. Rev. B: Condens. Matter Mater. Phys.* **2004**, *70* (21), 212101.
(28) Wu, X.; Holbig, E.; Steinle-Neumann, G. Structural Stability of TiO_2 at High Pressure in Density-Functional Theory Based Calculations. *J. Phys.: Condens. Matter* **2010**, *22* (29), 295501.
(29) Jedrzejczak, A.; Batory, D.; Cichomski, M.; Miletic, A.; Czerniak-Reczulska, M.; Niedzielski, P.; Dudek, M. Formation of Anatase and Srilankite Mixture as a Result of the Thermally Induced Transformation of the A-C:H:TiOx Coating. *Surf. Coat. Technol.* **2020**, *400*, 126230.
(30) McQueen, R. G.; Jamieson, J. C.; Marsh, S. P. Shock-Wave Compression and X-Ray Studies of Titanium Dioxide. *Science* **1967**, *155* (3768), 1401−1404.
(31) Smith, F. C.; Glass, B. P.; Simonson, B. M.; Smith, J. P.; Krull-Davatzes, A. E.; Booksh, K. S. Shock-Metamorphosed Rutile Grains Containing the High-Pressure Polymorph TiO_2-II in Four Neoarchean Spherule Layers. *Geology* **2016**, *44* (9), 775−778.
(32) Thevamaran, R.; Lawal, O.; Yazdi, S.; Jeon, S.-J.; Lee, J.-H.; Thomas, E. L. Dynamic Creation and Evolution of Gradient Nanostructure in Single-Crystal Metallic Microcubes. *Science* **2016**, *354* (6310), 312−316.
(33) Lee, S.; Cai, J.; Jin, S.; Zhang, D.; Thevamaran, R.; Xu, H. Coesite Formation at Low Pressure during Supersonic Microprojectile Impact of Opal. *ACS Earth Space Chem.* **2020**, *4* (8), 1291−1297.
(34) Cai, J.; Griesbach, C.; Thevamaran, R. Extreme Dynamic Performance of Nanofiber Mats under Supersonic Impacts Mediated by Interfacial Hydrogen Bonds. *ACS Nano* **2021**, *15* (12), 19945−19955.
(35) Cai, J.; Griesbach, C.; Ahnen, S. G.; Thevamaran, R. Dynamic Hardness Evolution in Metals from Impact Induced Gradient Dislocation Density. *Acta Mater.* **2023**, *249*, 118807.
(36) Toby, B. H.; Von Dreele, R. B. GSAS-II: The Genesis of a Modern Open-Source All Purpose Crystallography Software Package. *J. Appl. Crystallogr.* **2013**, *46* (2), 544−549.
(37) Perdew, J. P.; Wang, Y. Accurate and Simple Analytic Representation of the Electron-Gas Correlation Energy. *Phys. Rev. B: Condens. Matter Mater. Phys.* **1992**, *45* (23), 13244−13249.
(38) Wood, D. M.; Zunger, A. A New Method for Diagonalising Large Matrices. *J. Phys. A: Math. Gen.* **1985**, *18* (9), 1343−1359.
(39) Kresse, G.; Furthmüller, J. Efficient Iterative Schemes for Ab Initio Total-Energy Calculations Using a Plane-Wave Basis Set. *Phys. Rev. B: Condens. Matter Mater. Phys.* **1996**, *54* (16), 11169−11186.

(40) Blöchl, P. E. Projector Augmented-Wave Method. *Phys. Rev. B: Condens. Matter Mater. Phys.* **1994**, *50* (24), 17953−17979.
(41) Kresse, G.; Joubert, D. From Ultrasoft Pseudopotentials to the Projector Augmented-Wave Method. *Phys. Rev. B: Condens. Matter Mater. Phys.* **1999**, *59* (3), 1758−1775.
(42) Barnard, A. S.; Curtiss, L. A. Prediction of TiO_2 Nanoparticle Phase and Shape Transitions Controlled by Surface Chemistry. *Nano Lett.* **2005**, *5* (7), 1261−1266.
(43) Barnard, A. S. A Thermodynamic Model for the Shape and Stability of Twinned Nanostructures. *J. Phys. Chem. B* **2006**, *110* (48), 24498−24504.
(44) Kumar, P. S.; Kring, D. A. Impact Fracturing and Structural Modification of Sedimentary Rocks at Meteor Crater, Arizona. *J. Geophys. Res.: Planets* **2008**, *113* (E9), No. E09009.
(45) Bland, M. T.; Raymond, C. A.; Schenk, P. M.; Fu, R. R.; Kneissl, T.; Pasckert, J. H.; Hiesinger, H.; Preusker, F.; Park, R. S.; Marchi, S.; King, S. D.; Castillo-Rogez, J. C.; Russell, C. T. Composition and Structure of the Shallow Subsurface of Ceres Revealed by Crater Morphology. *Nat. Geosci.* **2016**, *9* (7), 538−542.
(46) Head, J. W.; Fassett, C. I.; Kadish, S. J.; Smith, D. E.; Zuber, M. T.; Neumann, G. A.; Mazarico, E. Global Distribution of Large Lunar Craters: Implications for Resurfacing and Impactor Populations. *Science* **2010**, *329* (5998), 1504−1507.
(47) Meagher, E. P.; Lager, G. A. Polyhedral Thermal Expansion in the TiO_2 Polymorphs; Refinement of the Crystal Structures of Rutile and Brookite at High Temperature. *Can. Mineral.* **1979**, *17* (1), 77−85.
(48) Howard, C. J.; Sabine, T. M.; Dickson, F. Structural and Thermal Parameters for Rutile and Anatase. *Acta Crystallogr., Sect. B: Struct. Sci.* **1991**, *47* (4), 462−468.
(49) Patterson, A. L. The Scherrer Formula for X-Ray Particle Size Determination. *Phys. Rev.* **1939**, *56* (10), 978−982.
(50) Cai, J.; Thevamaran, R. Superior Energy Dissipation by Ultrathin Semicrystalline Polymer Films Under Supersonic Microprojectile Impacts. *Nano Lett.* **2020**, *20* (8), 5632−5638.
(51) Hamad, S.; Catlow, C. R. A.; Woodley, S. M.; Lago, S.; Mejías, J. A. Structure and Stability of Small TiO_2 Nanoparticles. *J. Phys. Chem. B* **2005**, *109* (33), 15741−15748.
(52) Arroyo-de Dompablo, M. E.; Morales-García, A.; Taravillo, M. DFT+U Calculations of Crystal Lattice, Electronic Structure, and Phase Stability under Pressure of TiO_2 Polymorphs. *J. Chem. Phys.* **2011**, *135* (5), 054503.
(53) Zhu, T.; Gao, S.-P. The Stability, Electronic Structure, and Optical Property of TiO_2 Polymorphs. *J. Phys. Chem. C* **2014**, *118* (21), 11385−11396.
(54) Horn, M.; Schwebdtfeger, C. F.; Meagher, E. P. Refinement of the structure of anatase at several temperatures. *Z. Kristallogr.—Cryst. Mater.* **1972**, *136* (1−6), 273−281.
(55) Swope, R. J.; Smyth, J. R.; Larson, A. C. H in Rutile-Type Compounds: I. Single-Crystal Neutron and X-Ray Diffraction Study of H in Rutile. *Am. Mineral.* **1995**, *80* (5−6), 448−453.
(56) Sen, S.; Ram, M. L.; Roy, S.; Sarkar, B. K. The Structural Transformation of Anatase TiO_2 by High-Energy Vibrational Ball Milling. *J. Mater. Res.* **1999**, *14* (3), 841−848.
(57) Ren, R.; Yang, Z.; Shaw, L. L. Polymorphic Transformation and Powder Characteristics of TiO_2 during High Energy Milling. *J. Mater. Sci.* **2000**, *35* (23), 6015−6026.
(58) Dutta, H.; Sahu, P.; Pradhan, S. K.; De, M. Microstructure Characterization of Polymorphic Transformed Ball-Milled Anatase TiO_2 by Rietveld Method. *Mater. Chem. Phys.* **2003**, *77* (1), 153−164.
(59) Rezaee, M.; Mousavi Khoie, S. M.; Liu, K. H. The Role of Brookite in Mechanical Activation of Anatase-to-Rutile Transformation of Nanocrystalline TiO_2: An XRD and Raman Spectroscopy Investigation. *CrystEngComm* **2011**, *13* (16), 5055.
(60) Sepelák, V.; Bégin-Colin, S.; Caër, G. L. Transformations in Oxides Induced by High-Energy Ball-Milling. *Dalton Trans.* **2012**, *41* (39), 11927−11948.
(61) Penn, R. L.; Banfield, J. F. Formation of rutile nuclei at anatase (112) twin interfaces and the phase transformation mechanism in nanocrystalline titania. *Am. Mineral.* **1999**, *84* (5−6), 871−876.
(62) Beltrán, A.; Gracia, L.; Andrés, J. Density Functional Theory Study of the Brookite Surfaces and Phase Transitions between Natural Titania Polymorphs. *J. Phys. Chem. B* **2006**, *110* (46), 23417−23423.
(63) Xiaoyan, P.; Yi, C.; Xueming, M.; Lihui, Z. Phase Transformation of Nanocrystalline Anatase Powders Induced by Mechanical Activation. *J. Am. Ceram. Soc.* **2004**, *87* (6), 1164−1166.
(64) Gennari, F. C.; Pasquevich, D. M. Kinetics of the Anatase-Rutile Transformation in TiO_2 in the Presence of Fe_2O_3. *J. Mater. Sci.* **1998**, *33* (6), 1571−1578.
(65) Gouma, P. I.; Mills, M. J. Anatase-to-Rutile Transformation in Titania Powders. *J. Am. Ceram. Soc.* **2001**, *84* (3), 619−622.
(66) Hanaor, D. A. H.; Sorrell, C. C. Review of the Anatase to Rutile Phase Transformation. *J. Mater. Sci.* **2011**, *46* (4), 855−874.
(67) Su, R.; Bechstein, R.; Sø, L.; Vang, R. T.; Sillassen, M.; Esbjörnsson, B.; Palmqvist, A.; Besenbacher, F. How the Anatase-to-Rutile Ratio Influences the Photoreactivity of TiO_2. *J. Phys. Chem. C* **2011**, *115* (49), 24287−24292.
(68) Shannon, R. D.; Pask, J. A. Kinetics of the Anatase-Rutile Transformation. *J. Am. Ceram. Soc.* **1965**, *48* (8), 391−398.
(69) Shen, P.; Hwang, S. L.; Chu, H. T.; Yui, T. F.; Pan, C.; Huang, W. L. On the transformation pathways of α-PbO_2-type TiO_2 at the twin boundary of rutile bicrystals and the origin of rutile bicrystals. *Eur. J. Mineral.* **2005**, *17* (4), 543−552.
(70) Goresy, A. E.; Chen, M.; Dubrovinsky, L.; Gillet, P.; Graup, G. An Ultradense Polymorph of Rutile with Seven-Coordinated Titanium from the Ries Crater. *Science* **2001**, *293* (5534), 1467−1470.
(71) Wu, X.; Meng, D.; Han, Y. α-PbO_2-Type Nanophase of TiO_2 from Coesite-Bearing Eclogite in the Dabie Mountains, China. *Am. Mineral.* **2005**, *90* (8−9), 1458−1461.
(72) Shen, P.; Hwang, S.-L.; Chu, H.-T.; Yui, T.-F. α-PbO_2-Type TiO_2: From Mineral Physics to Natural Occurrence. *Int. Geol. Rev.* **2001**, *43* (4), 366−378.
(73) Guo, H.; Xu, H.; Barnard, A. S. Can hematite nanoparticles be an environmental indicator? *Energy Environ. Sci.* **2013**, *6* (2), 561−569.
(74) Motevalli, S. B.; Barnard, A. *QuickThermo. v1*; CSIRO. Software Collection, 2019.
(75) Thevamaran, R.; Griesbach, C.; Yazdi, S.; Ponga, M.; Alimadadi, H.; Lawal, O.; Jeon, S.-J.; Thomas, E. L. Dynamic Martensitic Phase Transformation in Single-Crystal Silver Microcubes. *Acta Mater.* **2020**, *182*, 131−143.

https://doi.org/10.1021/acsearthspacechem.3c00057
ACS Earth Space Chem. 2023, 7, 1905−1915